Visualization of local hydrogen diffusion in stainless steel using time resolved electron stimulated desorption

Naoya MIYAUCHI[a], Tomoya IWASAWA[a,b], Yoshiharu MURASE[a], Taro YAKABE[a], Masahiro KITAJIMA[a], Shoji TAKAGI[c], Tomomi AKIYAMA[d], Satoka AOYAGI[d] and Akiko N. ITAKURA[a*]

[a]*National Institute for Materials Science, 1-2-1 Sengen, Tsukuba, Ibaraki 305-0047, Japan*

[b]*University of Tsukuba, 1-1-1 Tennodai, Tsukuba, Ibaraki 305-8577, Japan*

[c]*Toho University, 2-2-1 Miyama, Funabashi, Chiba 274-8510, Japan*

[d]*Seikei University, 3-3-1 Kitamachi, Kichijoji, Musashino, Tokyo180-8633, Japan*

* itakura.akiko@nims.go.jp

Abstract

We have improved an electron stimulated desorption (ESD) apparatus to obtain the time evolution of hydrogen permeation for cold-worked stainless steel. Hydrogen permeation through grain structures was visualized by using the operando hydrogen microscope combining ESD and hydrogen supply system. The diffusion coefficients in grains were calculated from time evolution curves of hydrogen permeation. Principal component analysis (PCA) of hydrogen maps was used to classify crystal grains by the degrees of hydrogen diffusion and permeation flux. Grain structures such as the ratio of austenite/martensite, crystallographic orientations and coherent/random grain boundaries were determined by electron backscatter diffraction (EBSD) analysis. The areas with high-speed and high flux permeation of hydrogen were characterized as smaller austenitic

grains with grain boundaries. The usefulness of a combined ESD-PCA-EBSD analysis on hydrogen permeation in materials was demonstrated in the present study.

KEYWORDS; hydrogen diffusion, image analysis, electron stimulated desorption (ESD), electron backscattering diffraction (EBSD)

1. Introduction

Hydrogen embrittlement—along with corrosion—damages metal, which weakens the integrity of metal components and potentially endangers human life. Metallic materials such as stainless steels, in general, are not consisted of one single homogenous grain but polycrystal grains. Grain boundaries, which are interfaces, are classified according to the crystallographic consistency or orientation angle of adjacent crystal grains. In corrosion researches, corrosion susceptibility at grain boundary structures has been extensively studied for various materials, and materials having structures with high corrosion resistance have been developed. On the other side, although hydrogen embrittlement has been reported to occur in welded parts and places of local strain[1], the evaluation of initiation point of embrittlement has been limited for the broken sample. Visualization of hydrogen is technically difficult and is one of the major obstacles to the progress of hydrogen embrittlement research. Therefore, to determine the initiation point of hydrogen embrittlement, it is very important to determine the location and distribution of hydrogen in materials in real-time and under operando conditions.

In researches of hydrogen embrittlement, various methods have been utilised to detect the hydrogen diffusion in materials so far. Thermal desorption spectroscopy (TDS)[2], depth profiling by nuclear reaction analysis[3], hydrogen micro-print technique[4], secondary ion mass spectroscopy[5], and tritium autoradiography[6] are used for

hydrogen detection. Recently, Kelvin probe force microscopy[7, 8] has been applied, the technique requires special conditions of a pre-charged system to obtain high concentrations of hydrogen by the surface potential change. These techniques do not detect hydrogen directly or damage the sample. In contrast to them, electron stimulated desorption (ESD), a popular technique in surface science field to study adsorption or desorption physics and/or just find out adsorbate, is a powerful investigative tool for direct detection of hydrogen[9, 10] in a metal without damage. ESD utilizes probe electrons to stimulate an electron in bonding atom on the surface to anti-bonding state and be able to visualize the bonded position of the atom as a 2D image. In this paper, time dependent images of hydrogen permeation through a metal were obtained by ESD. In addition, principal component analysis (PCA) and electron backscatter diffraction (EBSD) analysis were also conducted in the same area examined by ESD. The purpose of this study is to propose the combined ESD-PCA-EBSD analysis as a useful method to evaluate the hydrogen permeation behaviour in materials.

2. Experimental

2.1 Method of hydrogen visualization

First, we will explain our hydrogen visualization system and the experimental conditions. We used original “operando hydrogen microscope” for the visualization [11, 12](**Fig. 1**). This system uses ESD to visualize the two-dimensional distribution of hydrogen on a surface, directly, not only of adsorbed hydrogen but also of hydrogen permeating through structural materials. Early studies for detection of hydrogen by ESD had been limited to the measurement of materials that could hold a lot of hydrogen for long time, such as hydrogen storage alloys[13, 14]. By adding a hydrogen supply system into UHV (Fig. 1-d), we are able to investigate dynamical hydrogen behaviour in

materials that do not contain large amount of hydrogen. Hydrogen supplied by the gas line is absorbed into the membrane-type sample from the rear side, diffuses through the sample, and exits on the UHV side. A tungsten filament of SEM (JUMP10, JEOL Co., Tokyo, Japan) was used for the ESD electron source. We have improved the background pressure to 10^{-8} Pa order and the stability of the electron beam of this apparatus in comparison with our previous paper [11]. As a result, the S/N of the ions and the spatial resolution of ion images were improved.

2.2 Sample preparation

The material used in the present study was 10% cold-worked SUS304 stainless steel. As-received material was annealed for 1 hour at 1373K to control grain size about 100 μm in diameter. The annealed material was rolled to 10% reduction in thickness at room temperature, aiming at introducing deformation-induced martensite. The cold-worked material was then spark-cut into a disk shape with 16 mm in diameter, followed by mechanical polishing and mirror-finishing on surface into the sample with a thickness of 100 μm in the center. Each grain size (50–150 μm) was measured with an optical microscope, close to the sample thickness (100 μm). The EBSD measurement provides the information of grain structures such as ratio of austenite/martensite, crystallographic orientations and coherent/random grain boundaries. During the experiment the temperature of the sample was kept at 473 K. In this case, hydrogen permeates through only one or two grains from the rear side to the UHV side which is at 10^{-8} Pa. Hydrogen atoms, permeating from the rear side of the sample to the UHV surface are desorbed by electron irradiation from the surface as hydrogen ions or as radical hydrogen atoms. Ions desorbed from each surface position, and the number of ions is proportional to hydrogen atoms existing on the surface in the case that the surface is a metal with uniform elements.

The surface was checked with energy dispersive X-ray spectrometry (EDX), confirming that the surface was uniform with elements of iron, chromium, nickel, oxygen, and a small amount of carbon contamination.

For determination of local and micro structures, measurement with EBSD was performed using a field emission microscope (JSM7900F, JEOL Co., Tokyo, Japan) equipped with a diffraction detector (EDAX-DVC-4). All data derived from EBSD measurements were analysed by OIM System (TSL Solutions Co., Kanagawa, Japan).

3. Result and discussion

3.1 Local hydrogen permeation and diffusion coefficient of each structure

One of the main results of the ESD experiment was the successful determination of local hydrogen permeation and diffusion coefficient of each structure.

3.1.1 Compare SEM image and hydrogen permeation mapping

Figure 2-a shows a SEM image of the sample and Figure 2-b shows a hydrogen map at the same position. The hydrogen distribution is integrated over 65 hours from the time that hydrogen was introduced to the rear side of the sample. With the understanding of this rough outline, austenite grains, which appeared as bright areas in the SEM image, were shown in the hydrogen map to be associated with large amounts of hydrogen. The dark grains including dislocations were found to have a relatively low presence of hydrogen. This trend was the same with previous research[11], but not a perfect match; there is a ring-shaped area indicated in the figure where presence of hydrogen was not well-related to grain type.

3.1.2 Separate crystalline by image fusion and principal component analysis

To extract the area and to calculate the local diffusion coefficients of each single grain, we classified the hydrogen map by a technique of principal component analysis

(PCA)[15]. The SEM image was rotated and shifted with respect to the hydrogen map, because the scan direction of incident electrons was slightly changed with the additional electric field used for ESD measurement. For PCA, we calibrated SEM and hydrogen maps by image fusion and adjusted the resolution and alignment of extraction locations at a 2000 × 2000 pixel level, which are the pixels of the hydrogen map. The following images were aligned and integrated as fusion image data for PCA: one SEM image, one hydrogen image before hydrogen supply from the rear side, and 13 hydrogen images, each of which was accumulated over 5 hours of ESD measurement until 65 hours. The PC1 image of PCA (Fig. 2-c) contains information of the SEM and ESD fusion image data (Figure 2-a and -b). The physical meaning of PC1 is that austenite grains have a higher volume of hydrogen permeation at later times in the permeation. The PC2 image (Fig. 2-d), which has the information from the fusion data, indicates the difference between the hydrogen maps and the SEM image. The PC3 image (Fig. 2-e) shows the difference between the earlier times and later times of hydrogen maps regardless of the SEM image. A ring pattern of a peculiar hydrogen distribution was observed throughout almost the entire measurement time, and it was confirmed to be one of features of the earlier time hydrogen maps.

3.1.3 Calculation of local diffusion coefficient of hydrogen in each crystalline type

Figure 3 shows the time evolution of ion counts from areas of austenite, martensite and the peculiar ring-shaped area. The areas used for counting were the pixels selected using the PCA results, and the ion counts were normalized to a value of counts/m^2. The reason for the large variation in Figure 3-c is that the measurement area was small. Two remarks can be derived from Figure 3. One is the diffusion coefficient of hydrogen at a

single structure, which can be obtained by fitting curves with formula (1) to ion counts with respect to time. Solid lines in the figure are the curves fitted by using Fick's law,

$$C(x,t) = C_0 \left[1 - \mathrm{erf}\left(\frac{x}{\sqrt{4Dt}}\right)\right] \quad (1)$$

$$D = D_0 \exp\left(-\frac{E_d}{RT}\right) \quad (2)$$

where C is concentration, C_0 is a constant, D is diffusion coefficient, D_0 is a constant (speed constant, hopping constant), E_d is activation energy, x is depth from the surface, (100 μm), R is gas constant (8.31 J/K/mol), and T is temperature. We obtained the diffusion coefficients and other parameters (the values of D, D_0 and E_d) from the fitting results shown in each figure. In addition, the curve in Figure 3-a could be resolved into two fitting components 1 and 2. Component 2 (blue line) shows similar fitting parameters of martensite (Figure 3-b), while component 1 (orange line) would be austenite. We consider that the austenite grains may have included dislocations. We checked the data from grains in each of the three different areas in Figure 3-a independently, and found that the height of the component 2 varied with each grain and sometimes component 2 did not appear. Grains that showed only the single component will be discussed below (in the section of 3. 2. 2). Our calculated diffusion coefficients (D) did not completely match the values of the reference data[16, 17]; however, they are consistent with the property of values for martensite being two orders of magnitude greater than values for austenite. The reason why our diffusion coefficients were smaller than those of the references may be because hydrogen was used for the permeation data in the references, whereas we used deuterium[5]. In addition, the reference data are not measured from a single crystalline, but are mean values of polycrystalline of a finite size together with grain boundaries. It is

considered that error in the diffusion coefficient of grains that have the same structure is derived from the difference in crystal orientation[18].

The other remark that can be derived from Figure 3 is that the amount of desorbed hydrogen differs between austenite and martensite structures. The double arrows on the right side of each figure show the amount of hydrogen permeation. We can say that hydrogen diffuses slowly in austenite but has a large amount of permeation. In dislocation included grain, hydrogen diffuses quickly and has a small amount of permeation. The permeation rate of hydrogen is proportional to the product of hydrogen solubility and the diffusion coefficient in the structure. The solubility of hydrogen in austenitic stainless steel is higher than the solubility of hydrogen in martensitic stainless steel[19], which is consistent with our results. In Figure 3-c, the volume through the ring area was almost the same as the permeation of austenite grains, especially that of component 1.

3.2 Discovery of a high-speed permeation path and the structure

3.2.1 High-speed and high flux permeation path

Next, we show the second major result, which is the discovery of a high-speed permeation path and its structure. Figure 2 includes a new information. The relationship between the ring pattern and the SEM image was unknown (see arrowed parts in Fig. 2-d and -e). The ring pattern was found to be emitted from not bright position in the SEM image from PC2 result, and the hydrogen distribution at the position of this ring continued to be high from the beginning of the permeation measurement to the end of the measurement from PC3 result. At the ring, the hydrogen diffusion coefficient is high and the amount of permeation is also high, which matches neither the hydrogen permeating properties of austenite nor that of martensite. Based on the PCA results, we succeeded in extracting the narrow area with new permeation properties that has not been previously

visualized. The diffusion coefficient of hydrogen would be different in structures, and crystal orientation[18] or a strains[19].

3.2.2 The structure of the high-speed and high flux permeation area

We focused on the areas in (1) and (2) in Figure 4-a, and tried to determine the structure of the areas with high-speed and high flux permeation area by using EBSD measurement. The inverse pole figure map in wide area for austenite revealed that the orientation of the central green grain (Fig. 4-b) was austenite (101), and the austenite structure ratio was 97% or more. This is the grain showing the single fitting component of the diffusion coefficient that we discussed at Figure 3. The other grains that looked to be mix structure of austenite and martensite show the permeation properties of martensite together with austenite. On the other hand, the upper right grain, in which a martensite structure ratio was 70%, did not show the permeation properties of austenite (Fig. 3-b), despite including 30% austenite. This indicates that the influence of martensite on permeation was too dominant to detect that of austenite. As shown in Figures 4-1b and -2b, high-resolution EBSD images show the smaller austenite grains and grain boundaries in areas of (1) and (2). In Figure 4-1c, it can be seen that the hydrogen distribution showing the ring shape in area (1) may be related to grain boundaries including Σ3 coherent grain boundaries. Since the dislocation slips were severely overlapped at the grain boundaries, these grain boundaries could not be characterized only with Σ3. In area (2), although the relationship between hydrogen distribution and Σ3 coherent grain boundaries was less significant than that in area (1), small austenite grains with multiple orientations and grain boundaries were observed similarly to area (1). The role of grain boundaries on hydrogen permeation has been investigated by many researchers [20-24], but there are still contradiction about its role between promotion [20-22] and suppression [23, 24]. In our former research [11],

the lower permeation volume has been detected at grain boundaries. Recent study has reported that the coherent grain boundary Σ3 of Ni offers a quick diffusion path for hydrogen[20]. In the present study, the high-speed and high flux permeation were detected in areas of (1) and (2) containing smaller austenite grains and grain boundaries. Therefore, it is suggested that the high-speed and high flux permeation of hydrogen would be sustained by the coexistence of a high diffusion coefficient of grain boundaries and supply of hydrogen from the surrounding austenite grains.

3.3 Summary of experimental result

We have separated and characterized hydrogen diffusion at grain boundaries by using an operando hydrogen microscope. Calculations were conducted by assuming hydrogen permeation was in a single direction. To understand the diffusion in the ring area (high-speed and high flux permeation), it is necessary to consider the following lateral hydrogen paths through the membrane sample: bidirectional transfers from austenite grains to the grain boundary and from the grain boundary to the crystal. In the present study, the spatial resolution of the hydrogen maps was about only 1 μm, but it is meaningful that the discussion of hydrogen permeation was effectively supported by PCA and EBSD analysis to embark on this difficult problem. Thus, the usefulness of a combined ESD-PCA-EBSD analysis was demonstrated to improve the understanding of hydrogen permeation in materials in the present study.

4. Conclusions

Time evolution of hydrogen permeation in grain structures for cold-worked stainless steel was examined by using ESD. Subsequently, the discussion of hydrogen permeation was supported by PCA and EBSD analysis. The new findings are:

1) Time dependence of ion counts in each type of grain was obtained by ESD. Evolution curves of hydrogen permeation in grains were discussed on the fitting with the Fick's law.
2) SEM image and time-resolved ESD images were comparatively examined by PCA to pick up the areas with high-speed and high flux permeation of hydrogen.
3) The information of grain structures (ratio of austenite/martensite, crystallographic orientations and coherent/random grain boundaries) was obtained by EBSD analysis. Small austenite grains with boundaries were mainly detected in the areas with high-speed and high flux permeation of hydrogen.
4) The higher-speed and high flux permeation of hydrogen in the areas would be sustained by the coexistence of a high diffusion coefficient of grain boundaries and supply of hydrogen from the surrounding austenite grains. The usefulness of a combined ESD-PCA-EBSD analysis was demonstrated to improve the understanding of hydrogen permeation in materials in the present study.

Acknowledgments

We thank Dr. Masahiro Tosa, Dr. Daisuke Fujita, and Dr. Chikashi Nishimura of the National Institute for Materials Science (NIMS), and Prof. Eiji Akiyama of Tohoku University for their invaluable discussions and for sharing their important knowledge of metal science and hydrogen physics. This research was supported by a MEXT/JSPS KAKENHI grant (Grant number JP 18H03849).

References

[1] M. Hatano, M. Fujinami, K. Arai, H. Fujii, M. Nagumo, Hydrogen embrittlement of austenitic stainless steels revealed by deformation microstructures and strain-induced creation of vacancies, Acta Materialia 67 (2014) 342-353.

[2] A.N. Itakura, M. Tosa, T. Yakabe, N. Miyauchi, A. Kasahara, T. Miyata, T. Shindo, Low Outgas Surface Treatment of Stainless Steel 316L Using Segregated Chromium Oxide Layer, Vacuum and Surface Science 61 (2018) 675-680.
[3] M. Wilde, K. Fukutani, Hydrogen detection near surfaces and shallow interfaces with resonant nuclear reaction analysis, Surf. Sci. Rep. 69 (2014) 196–295.
[4] T.E. Perez, J. Ovejero-Garcia, Direct observation of hydrogen evolution in the electron microscope scale, Scripta Metallurgica 16 (1982) 161-164.
[5] O. Sobol, F. Straub, T. Wirth, G. Holzlechner, T. Boellinghaus, W.E.S. Unger, Real Time Imaging of Deuterium in a Duplex Stainless Steel Microstructure by Time-of-Flight SIMS, Scientific Reports 6 (2016) 19929.
[6] T. Asaoka, G. Lasasset, M. Aucouturier, P. Lacombe, Observation of Hydrogen Trapping in Fe-0.15 Wt% Ti Alloy by High Resolution Autoradiography, Corrosion Science 34 (1978) 39-47.
[7] C. Larignon, J. Alexis, E. Andrieu, L. Lacroix, G. Odemer, C. Blanc, Combined Kelvin probe force microscopy and secondary ion mass spectrometry for hydrogen detection in corroded 2024 aluminium alloy, Electrochimica Acdta 110 (2013) 484-490.
[8] S. Evers, C. Sen¨oz, M. Rohwerder, Hydrogen detection in metals: a review and introduction of a Kelvin probe approach, Science and Technology of Advabced Materials 14 (2013) 014201.
[9] D. Menzel, R. Gomer, Desorption from Metal Surfaces by Low - Energy Electrons, The Journal of Chemical Physics 41 (1964) 3311.
[10] I. Yagi, K. Ogai, T. Kondo, A. Fujishima, K. Ueda, K. Uosaki, Direct Proof for Electrochemical Substitution of Surface Hydrogen of Boron-doped Diamond Electrode by TOF-ESD Method, Chemistry Letters 32 (2003) 1050-1051.
[11] N. Miyauchi, K. Hirata, Y. Murase, H.A. Sakaue, T. Yakabe, A.N. Itakura, T. Gotoh, S. Takagi, 2D mapping of hydrogen permeation from a stainless steel membrane, Scripta Materialia 144 (2018) 69-73.
[12] N. Miyauchi, T. Iwasawa, Y. Murase, S. Takagi, A.N. Itakura, Observation of metal surface by operando hydrogen microscope, Vacuum and Surface Science 62 (2019) 27-32.
[13] S. Takagi, T. Goto, Observation of a titanium surface by desorbed ion images with a scanning electron microscope, Surface Science 287/288 (1993) 361-365.
[14] Y. Itoh, K. Ueda, Hydrogen and oxygen behaviors on Porous-Si surfaces observed using a scanning ESD ion microscope, Applied Surface Science 237 (2004) 596-601.
[15] K. Takahashi, T. Yamagishi, S. Aoyagi, D. Aoki, K. Fukushima, Y. Kimura, Principal component analysis image fusion of TOF-SIMS and microscopic images and low intensity secondary ion enhancement by pixel reduction, Journal of Vacuum Science & Technology B

36 (2018) 03F113.
[16] S. Xiukui, X. Jian, L. Yiyi, Hydrogen permeation behaviour in austenitic stainless steels Materials Science and Engineering: A 114 (1989) 179-187.
[17] J. Xu, X.Z. Yuan, X.K. Sun, B.M. Wei, Hydrogen permeation and diffusion in a 0.2C–13Cr martensitic stainless steel, Scripta Metallurgica et Materialia 29 (1993) 925-930.
[18] Z. Hua, B. An, T. Iijima, C. Gu, J. Zheng, The finding of crystallographic orientation dependence of hydrogen diffusion in austenitic stainless steel by scanning Kelvin probe force microscopy, Scripta Materialia 131 (2017) 47-50.
[19] J. Volkl, G. Alefeld, Hydrogen in Metals in: Y.P. Lee, P.M. Ossi (Eds.) Topics in Applied Physics, Springer-Verlag Berlin Heidelberg, Heidelberg & N. Y., 1978, p. 428.
[20] Z.X. Ma, X.L. Xiong, L.N. Zhang, Z.H. Zhang, Y. Yan, Y.J. Sua, Experimental study on the diffusion of hydrogen along individual grain boundaries in nickel, Electrochemistry Communications 92 (2018) 24-28.
[21] Y. Mine, K. Tachibana, Z. Horita, Mater. Sci. Eng. A 528 (2011) 8100-8105.
[22] R.D. Calder, T.S. Elleman, K. Verghese, J. Nucl. Mater 46 (1973) 46-52.
[23] J. Yao, J.R. Cahoon, Acta Metall. Mater 39 (1991) 119-126.
[24] W. Beck, J.O.'M. Bockris, J. McBreen, L. Nanis, Proc. R. Soc. A 290 (1966) 220-235

Figures and Captions

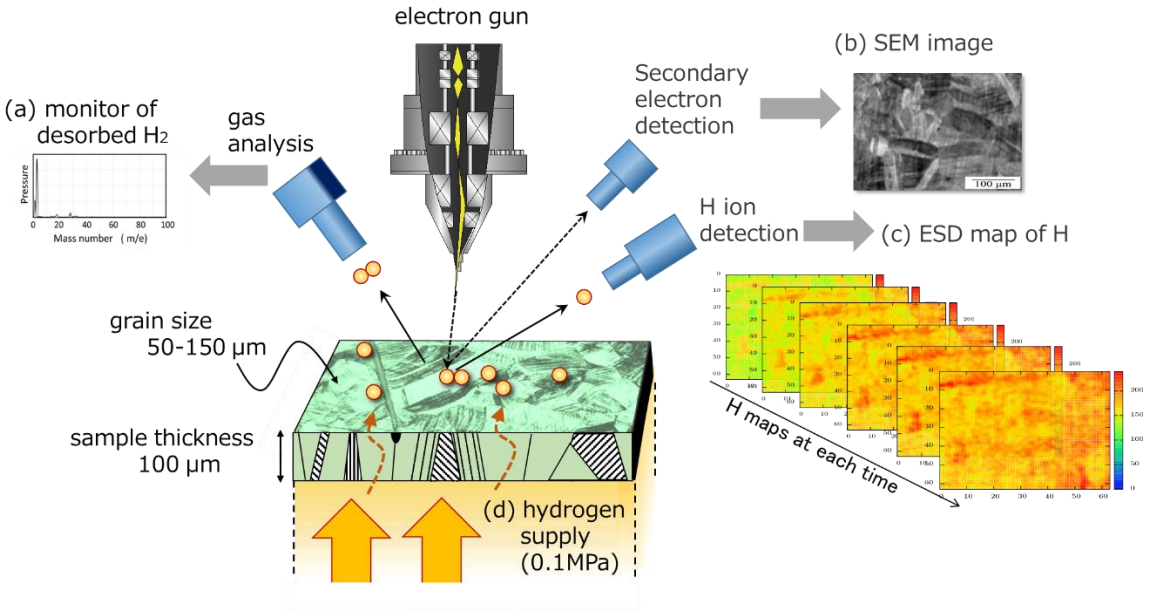

Figure 1. Schematic diagram of experimental setup of the operando hydrogen microscope. **(a)** Residual gas in the UHV chamber is monitored by quadrupole mass spectrometer. It was confirmed that 99% of the gas that increased during the permeation experiment was hydrogen. **(b)** SEM images are taken with the signal of the secondary electron detector before and after the hydrogen permeation experiment. **(c)** Hydrogen maps are created from ESD ions in real time detected by pulse counting in the channel plate together with information on the position of desorption. We chose an electron energy of 1000 eV, with an imaging time of 400 seconds and an interval time of 50 seconds for each frame of a 330 μm × 520 μm map. Maps are created continuously during the permeation experiment. SEM images and ESD maps are created by scanning electron beam using the same electron gun. **(d)** Hydrogen supply for long period measurement. The sample is vacuum sealed to a hydrogen gas line introducing hydrogen gas into a UHV chamber. Hydrogen is absorbed into the sample from the rear side, diffuses through the sample, and exits into the UHV chamber. In this experiment we have used 0.1MPa deuterium to separate from residual gas in UHV chamber.

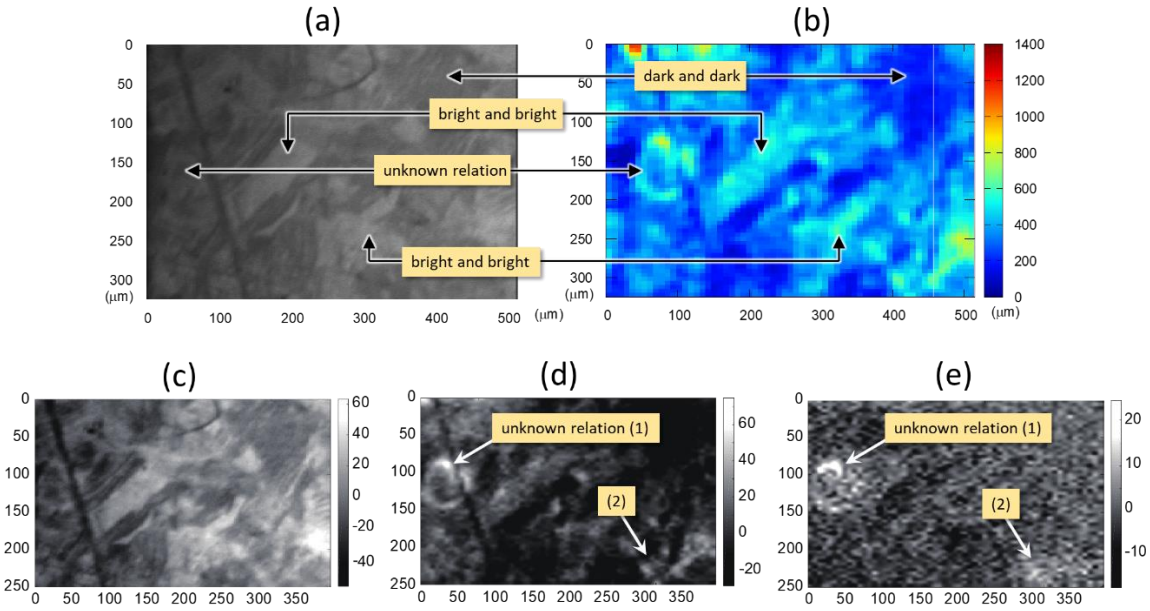

Figure 2. SEM image and hydrogen map of SUS304 including dislocations and the comparison result with PCA at 473 K. **(a)** SEM image of 330 μm × 520 μm. **(b)** Hydrogen distribution at the same position as (a). The colour bar indicates the hydrogen ion count at each position. The ion counts are integrated over 65 hours from when hydrogen was introduced to the rear side of the sample. Arrows with comments are points of interest. There are many grains or areas where the brightness distribution of the SEM image and the hydrogen map match. However, there are some areas of unknown relationship, where the brightness does not match. (c) PC1 score image, which contains 55.26% information of the SEM and DIET fusion image data. It corresponds to the SEM image and hydrogen maps. The physical meaning is that the bright austenite grains in SEM have higher volume of hydrogen permeation. (d) PC2 score image, which has 28.33% information from the fusion data, indicates the difference between the hydrogen maps and the SEM image. The image extracts the high hydrogen distribution area of unknown relation with SEM brightness, arrowed as examples the ring shape area (1) and lower right area (2). (e) PC3 score image, which has 2.57% information of the fusion data, shows the difference between the earlier time and later time of hydrogen maps regardless of the SEM image. It is shown the peculiar area (1) and (2) in PC3, too.

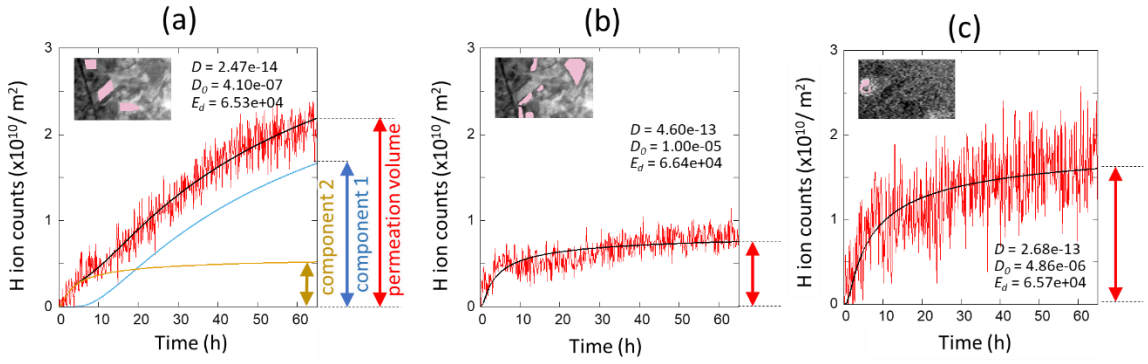

Figure 3. Time dependence of ion counts in each type of grain. Counts are calibrated to the number per unit area. **(a)** Time evolution of ion counts desorbed from austenite grains. For the austenite area, 452 pixels were chosen from within the bright grains in the PC1 image (coloured parts in the inserted image). **(b)** Time evolution of ion counts from grains including dislocations. 659 pixels from the PC1 image were chosen as areas including the dislocations. **(c)** Ion counts from the peculiar part, the ring area (1). Only 105 pixels chosen from the PC3 image were used for the peculiar area. Solid black lines in the figures are curves fitted using Fick's law. The fitting results are shown in each figure. Only the ion count line in (a) can be resolved into two fitting components. Component 1 (blue line) has a slow diffusion speed and Component 2 (orange line) has a faster diffusion speed. The red double arrow on the right side of each figure shows the amount of hydrogen permeation at 65 hours. For (a) only, the amount of permeation when resolved into two components is also inserted. It can be seen that it is about 2.2×10^{10} counts/m^2 and can be separated into 1.7×10^{10} counts/m^2 and 5.2×10^{9} counts/m^2. In (b) the hydrogen count at grains including dislocations was about 7.6×10^{9} counts/m^2. In (c), the count through the ring area was about 1.6×10^{10} counts/m^2.

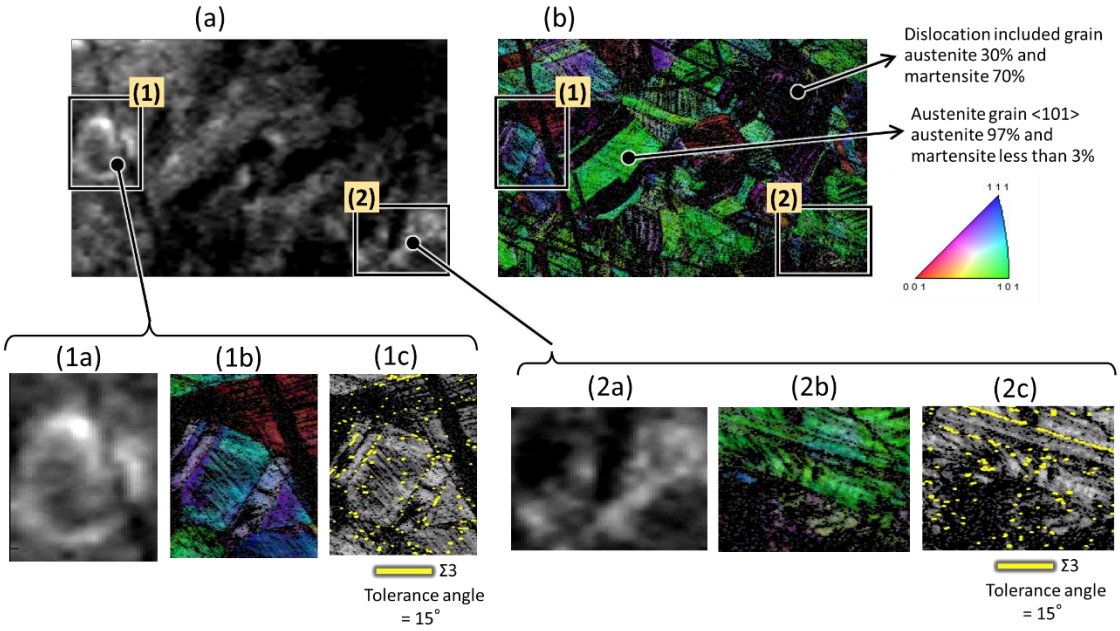

Figure 4. EBSD result measured after the hydrogen permeation experiment. **(a)** PC3 in PCA. Arrows indicate the areas of interest, which are areas with peculiar permutation properties. **(b)** Low-resolution (1 µm steps) inverse pole figure map for austenite over the whole the area of (a). Colour scale indicating the crystal orientation is shown to the side. (1b and 2b) High-resolution measurement of austenite orientation of areas (1) and (2). (1c and 2c) Distribution of coherent grain boundaries of type Σ3. The tolerance angle of Σ3 is 15°. The tolerance angle of Σ3 is usually taken to be 8.66°, but we used 15° since the sample was a cold-rolled sample and a large allowable angle was taken in consideration of local distortion.